Received: 8 July 2020 | Revised: 25 August 2020 | Accepted: 1 September 2020

DOI: 10.1002/ppap.202000140

FULL PAPER

PLASMA PROCESSES AND POLYMERS

Plasma-based VAD process for multiply doped glass powders and high-performance fiber preforms with outstanding homogeneity

Tom Trautvetter[1] | **Jan Schäfer**[2] | **Omar Benzine**[3] | **Ralf Methling**[2] | **Hardy Baierl**[1] | **Volker Reichel**[1] | **Jan Dellith**[1] | **Daniel Köpp**[2] | **Frank Hempel**[2] | **Marjan Stankov**[2] | **Margarita Baeva**[2] | **Rüdiger Foest**[2] | **Lothar Wondraczek**[3] | **Katrin Wondraczek**[1] | **Hartmut Bartelt**[1]

[1]Fiber Research and Technology, Leibniz Institute of Photonic Technology, Jena, Germany

[2]Plasma Surface Technology, Leibniz Institute for Plasma Science and Technology, Greifswald, Germany

[3]Laboratory of Glass Science, Otto Schott Institute of Materials Research, Jena, Germany

Correspondence
Tom Trautvetter and Katrin Wondraczek, Leibniz Institute of Photonic Technology, 07745 Jena, Germany.
Email: tom.trautvetter@leibniz-ipht.de (T. T.) and katrin.wondraczek@leibniz-ipht.de (K. W.)

Funding information
H2020 European Research Council, Grant/Award Numbers: ERC grant UTOPES, Grant Agreement No. 681652; Leibniz-Gemeinschaft, Grant/Award Number: SAW Excellence Research Competition

Abstract

An innovative approach using the vapor axial deposition (VAD), for the preparation of silica-based high-power fiber laser preforms, is described in this study. The VAD uses a plasma deposition system operating at atmospheric pressure, fed by a single, chemically adapted solution containing precursors of laser-active dopants (e.g., Yb_2O_3), glass-modifier species (e.g., Al_2O_3), and the silica matrix. The approach enables simultaneous doping with multiple optically active species and overcomes some of the current technological limitations encountered with well-established fiber preform technologies in terms of dopant distribution, doping levels, and achievable active core diameter. The deposition of co-doped silica with outstanding homogeneity is proven by Raman spectroscopy and electron probe microanalysis. Yb_2O_3 concentrations are realized up to 0.3 mol% in SiO_2, with simultaneous doping of 3 mol% of Al_2O_3.

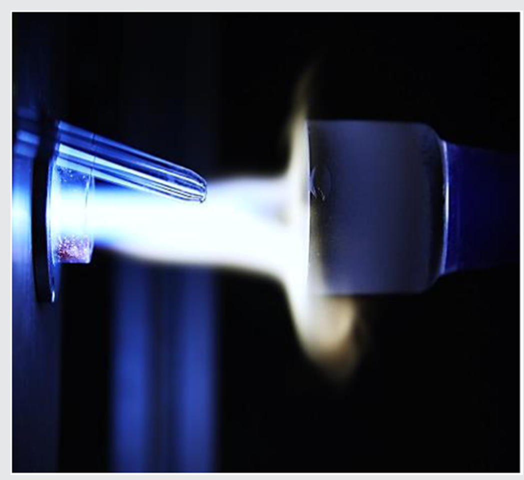

KEYWORDS

atmospheric pressure, dopant homogeneity, microwave plasma, preform fabrication, silica

Abbreviations: BO, bridging oxygen; EPMA, electron probe microanalysis; MCVD, modified chemical vapor deposition; NA, numerical aperture; OES, optical emission spectroscopy; OMCTS, octamethylcyclotetrasiloxane; RE, rare earth; Repusil, reactive powder sintering technology; SBS, stimulated Brillouin scattering; SRS, stimulated Raman scattering; TEOS, tetraethoxysilane; VAD, vapor axial deposition.

This is an open access article under the terms of the Creative Commons Attribution License, which permits use, distribution and reproduction in any medium, provided the original work is properly cited.

© 2020 The Authors. *Plasma Processes and Polymers* published by Wiley-VCH GmbH

1 | INTRODUCTION

The scaling to higher power levels for laser fibers with an excellent beam quality is limited by parasitic nonlinear effects, like stimulated Raman scattering (SRS) and stimulated Brillouin scattering (SBS). The basic concept to maintain a single-mode operation with an excellent beam quality is to use a small fiber core with a low numerical aperture (NA; low refractive index, respectively).[1,2] On the downside, such approaches require higher dopant levels while maintaining high uniformity in dopant distribution.[3–5] This poses a serious technological problem, whereby the spatial homogeneity of the dopant concentration is limited as a result of chemical clustering, phase separation and segregation, dissolution reactions, and low diffusion rates. The delicate interplay between matrix chemistry, dopant properties, and processing conditions imposes relatively narrow windows on achievable active core specifications in terms of dopant distribution, maximum dopant concentration, and core diameter.[6,7]

Established high-temperature preform fabrication technologies such as modified chemical vapor deposition (MCVD),[8,9] reactive powder sintering technology (Repusil),[10] or conventional glass melting[11] face limitations in amount and composition of dopant incorporation in silica due to diffusion-controlled processes and phase equilibria. The incorporation of multiple refractive index changing dopants into the silica glass matrix typically consists of several subsequent steps, each imposing additional thermal history on the doped samples, and thus impacting the overall homogeneity of the core material in sometimes counteracting ways.

Incorporating dopants during the formation of a silica network in an all-liquid state while circumventing deposition from the vapor phase on solid soot or in particle suspension opens an alternative route. Here, the sol–gel technology based on liquid silane solutions (combined with virtually arbitrary additive precursors) allows for an easy-to-handle process, yielding highly crosslinked and homogeneous materials of complex chemistry. Nevertheless, post-process vitrification of such crosslinked materials is required, again calling for an auxiliary thermal processing step that impacts the resulting glass preform. Fibers drawn from such processed preforms still exhibit a high OH content and residual carbon, limiting fiber quality, for example, fiber attenuation properties.[12–15]

To overcome current technological boundaries in terms of rare-earth (RE) doping levels, RE dopant homogeneity as well as active core diameter, a microwave plasma-based approach in a vapor axial deposition (VAD) configuration was developed for an all-liquid precursor injection solution using liquid organic precursors for deposition. The plasma-based method provides a nonequilibrium thermodynamic approach paired with a kinetic-controlled process in which diffusion limits are overruled. Effects such as phase separations and crystallization effects often encountered in thermal equilibrium states at high RE doping levels can thus be suppressed. The approach enables deposition of multiple dopants within a single processing step.

2 | EXPERIMENTAL SETUP

2.1 | Plasma source

The application of plasma systems operated at atmospheric pressure offers a variety of advantages such as a high density of active species, resulting in higher reaction rates and thus a significant increase of the deposition rates and efficiencies, compared with low-pressure plasmas. Recent research studies have shown that plasma technology working at atmospheric pressure is a valuable tool for the treatment of specialty optical fibers.[16,17] Furthermore, those systems are favored for industrial applications due to their scalability, cost-effectiveness, and swift system integration into inline processes.[18–21]

A microwave plasma source as an electrodeless system was selected for circumventing incorporation of electrode contaminations into the preform material, as encountered with DC/AC plasma jets.[22] Moreover, microwave plasmas come across highly increased intrinsic electron, ion, and radical densities, that is, enhanced deposition efficiencies as compared with other plasma sources, making it superior for fiber preform fabrication.[23,24]

2.2 | Microwave plasma jet

The setup shown in Figure 1 consists of a microwave source (Mügge GmbH), working at a frequency of 2.45 GHz with a maximum power level of 3 kW. For adjusting the coupling parameters, the maximum electric field of the standing microwave can be shifted within a rectangular waveguide R26, which is connected to peripheral attachments (adjustable waveguide section, shorting plunger, rod tuner). Optimization of setup parameters was carried out using the fundamental microwave TE_{10} mode. A more detailed description of the system and its optimization has been provided recently.[25,26]

2.3 | Precursor injection system

The deposition of doped SiO_2 using an all-liquid precursor injection solution requires a uniform droplet size

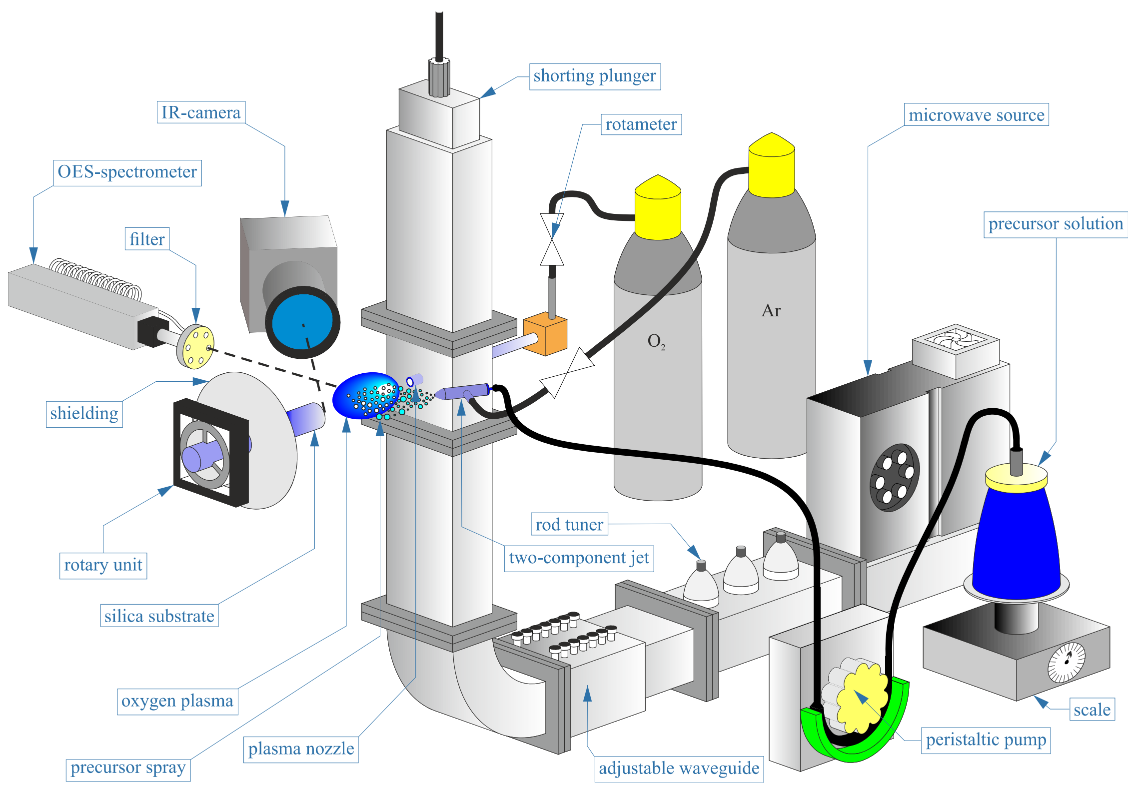

FIGURE 1 Vapor axial deposition setup, including the microwave plasma jet and auxiliary components

of the injected solution within the plasma zone using an appropriate gas flow. This will allow for a controlled pyrolysis in a defined plasma zone, creating fully oxidized nanoparticles for deposition.

The injection system consists of a two-component jet setup, allowing for separate channels and thus adjustment for liquid precursor and gas injection flow. This renders the jet system less susceptible to clogging due to active cooling of the precursor (preventing thermal decomposition). However, the viscosity of the liquid can be higher than in single-component jets due to the extra amount of kinetic energy provided by the external gas flow that causes an efficient nebulization.[27]

2.4 | Precursor materials

To achieve a uniform distribution of all dopants within the silica host on a microscopic scale, it is necessary to avoid spraying of multiple liquids into the active zone susceptible to core shell formation due to different condensation kinetics imposed by different melting points of dissolved components.[27] Therefore, a one-pot process was elaborated so as to provide for the required homogeneity of the precursor injection solution. The solution consisted of an organic silane for the silica matrix, dissolved dopant salts, acid for pH adjustment to a pH value of 2, deionized water, and ethanol: TEOS (tetraethoxysilane, $Si(OC_2H_5)_4$, 99.9%; Alfa Aesar), $Al(NO_3)_3 \cdot 9H_2O$ (98%; Alfa Aesar), $Yb(NO_3)_3 \cdot 5H_2O$ (99.9%; Sigma-Aldrich), and HNO_3 (68%; Sigma-Aldrich), respectively. The molar ratio for Al:Yb was set to 10:1, which is known to prevent clustering of RE species in silica-based materials.[28,29] To adjust viscosity and surface tension of the solution, ethanol (99.8%; Alfa Aesar) was added.

For initial setup configuration, to investigate optimal deposition parameters, undoped octamethylcyclotetrasiloxane (OMCTS, $C_8H_{24}O_4Si_4$ 99.99%; Heraeus) was used.

2.5 | Online optical emission spectroscopy (OES)

To investigate the influence of various input parameters on plasma emissions and thus deposition characteristics, online measurement periphery was installed, comprising OES and an imaging spectrograph (Roper Acton) combined with an intensified CCD camera (PI-MAX4:1024i-RB; Princeton Instruments). The emission from the plasma zone is focused by a quartz lens placed behind an iris 300 mm from the active plasma region and is coupled with a UV–VIS fiber connected to the spectrograph.

The spectrograph consists of three different gratings with 50, 600, and 2400 lines/mm, respectively, providing a spectral resolution of 0.03 nm and allowing to record molecular band

structures. Furthermore, cut-off filters were inserted between the coupling optics and the UV-VIS-fiber to suppress spectral lines of higher orders, if necessary.

The measurements were performed at three different positions, *x*, along the axis between plasma nozzle and substrate at a distance of 5 mm. The plasma generation is provided using 1 kW of applied microwave power coupled with an oxygen flow with a rate of 10 slm. An upscaling to 3-kW microwave power increased the emitted intensities, but it did not affect the overall spectral distribution. The injection of precursor material always occurred at an angle of 45°.

2.6 | Online infrared (IR) camera measurements

For substrate temperature measurements during plasma deposition, an IR camera (VarioCAM by InfraTec) with an effective resolution of 640 × 480 pixels has been utilized. The calibrated temperature range was set between 720 and 1770 K by the manufacturer, but surface temperature measurements above 2000 K were also allowed.

2.7 | Electron probe microanalysis (EPMA) analysis

For quantitative elemental analyses, an electron probe microanalyzer (JXA 8800L; JEOL) was applied using wavelength-dispersive spectroscopy. To verify chemical homogeneity of the samples, a line scan along a sample cross-section using a step size of 50 µm was done. Moreover, a backscattered electron (BSE) detector was used to visualize material contrast.

2.8 | Raman spectroscopy

In addition to EPMA analysis, structural investigations were conducted by Raman spectroscopy (Renishaw™) via line scans (×50 objective, 514.5-nm Argon laser for excitation, step size 15 µm) across the sample diameter of 2 mm. The Raman signal was collected with a CCD camera in the range of 120–1375/cm with an effective spectral resolution of 2/cm.

2.9 | Brunauer–Emmett–Teller (BET) surface area measurement

For determination of porosity and specific surface area of the plasma-processed samples, BET measurements were conducted using the analyzer Tristar 3000 (Micromeritics GmbH, Germany).

3 | RESULTS AND DISCUSSION

Results of OES and IR camera measurements during the deposition process are presented and discussed. The deposition results of the plasma-processed samples are evaluated in terms of homogeneity using EPMA and Raman spectroscopy data.

3.1 | Results of OES

To validate and refine the plasma model as derived in Baeva et al.,[30] and for fundamental understanding of excitation and fragmentation processes occurring in the plasma, online OES measurements during deposition were carried out. The acquired OES spectra from pure oxygen plasma mixed with argon from the two-component jet allow retrieving optimum working distance by extraction of decomposition length across the active plasma zone as a function of plasma parameters. In general, a low working distance creates higher surface temperatures on the substrate, having a positive effect on densification. However, this may also cause a deposit that might be carbon-contaminated due to insufficient decomposition time. However, an increase of the working distances would lead to an improved decomposition of the precursor, though, unfortunately, related to lower substrate temperatures being susceptible to only partial vitrification.

Next, the incorporation of undoped OMCTS into the plasma plume is presented for varying precursor loads. Previous experiments with TEOS have shown a similar spectral composition, but with lower emission intensities as compared with OMCTS-containing plasmas.[25] For adjustment of the optimal working distance and material flow rate, OMCTS proved to be a suitable choice. In Figure 2, exemplary spectra are shown for the case of pure oxygen plasma (from the plasma nozzle) mixed with varying OMCTS loads (from the two-component jet).

At a distance of $x = 5$ mm (Figure 2a), the OES spectra are dominated by the oxygen plasma itself. In the UV wavelength range, the Schumann–Runge system of molecular oxygen dominates; however, the strongest emission at wavelengths below 200 nm cannot be detected by the current OES setup.[31,32] With increasing precursor load, a decrease in the intensity of the Schumann–Runge system is observed, accompanied by an increase of the C_2 Swan system of molecular carbon. This indicates the presence of less excited molecular oxygen species, but more excited

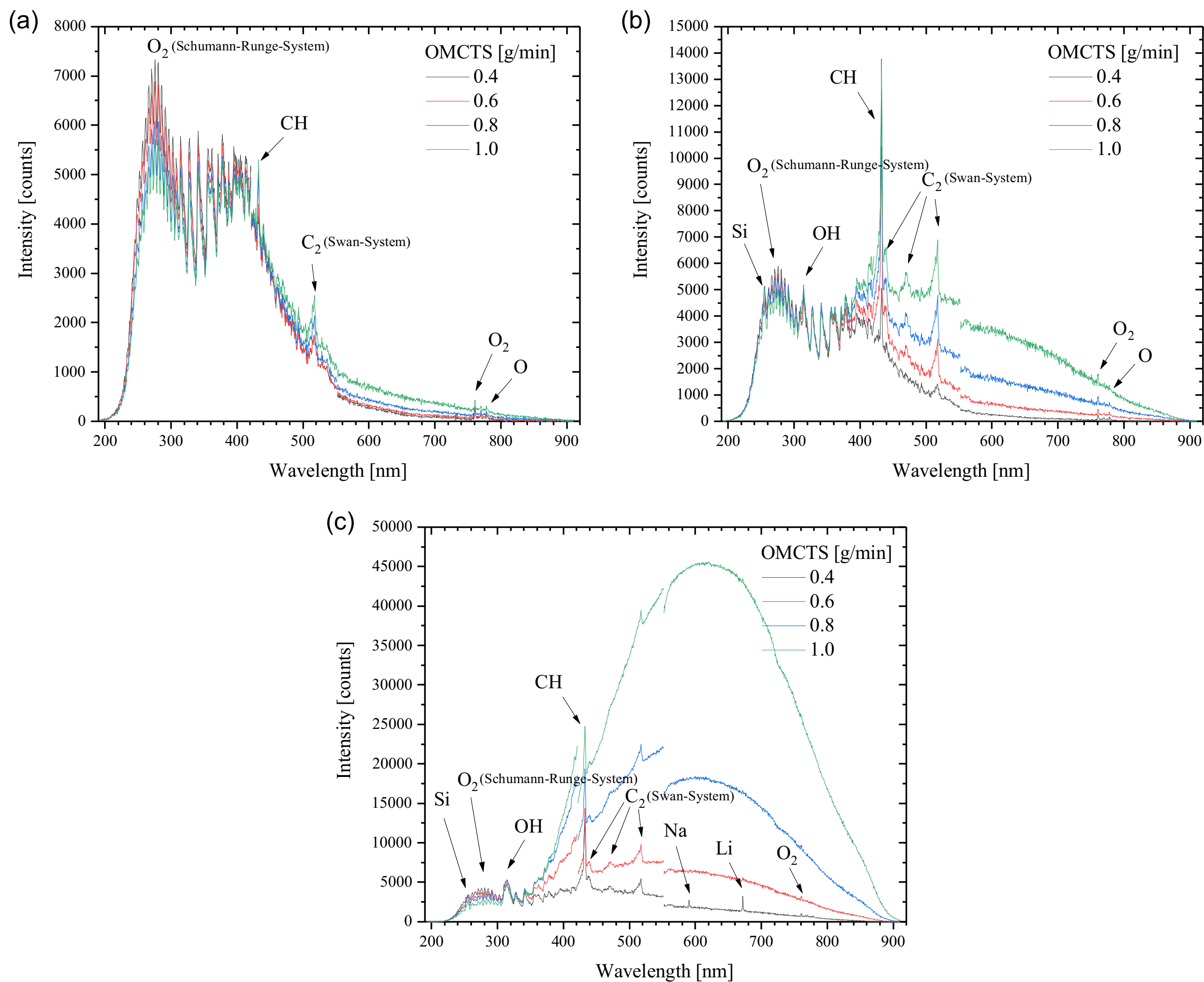

FIGURE 2 Optical emission spectra obtained for a microwave power of 1 kW from pure oxygen plasma with a flow rate of 10 slm at a distance (from the nozzle) of (a) $x = 5$ mm, (b) $x = 10$ mm, and (c) 15 mm. OMCTS, octamethylcyclotetrasiloxane

decomposition products of the organic precursor. Increasing the distance to $x = 10$ mm (Figure 2b) amplifies the intensities of the C_2 Swan system, which is attributed to the expanded zone where precursor and the oxygen plasma are mixed together. Also observable are the OH emission bands originating from diffusion of water from ambient air into the plasma zone, and the Si emission from the increased OMCTS decomposition, which is absent in Figure 2a. At an even larger distance, that is, $x = 15$ mm, atomic lines of Na and Li are observed originating from trace contamination of glass substrates in the range of ppb, as indicated by additional experiments. Most relevant for an efficient VAD process is the prominent feature at wavelengths above 500 nm, caused by accelerated precursor decomposition, where a huge continuum is formed, as shown in Figure 2c. In this region and above $x = 15$ mm, optimal precursor decomposition is indicated, which is a valid measure for carbon-free, efficient deposition.

The spectral analysis unfolds as a suitable tool for inline optimization of the deposition process by suppressing the contamination while adjusting the optimal working distance.

3.2 | Results of IR camera measurements

According to online IR camera measurements, the maximum achieved substrate temperature during deposition was at around 1100°C for a working distance of 50 mm. Previous research has shown that for this setup configuration, working distances below and above 50 mm render unfavorable due to geometric and fluid mechanic constraints (nozzle geometry, strong cooling by two-component jet). In Figure 3, substrate temperature as a function of working distance with the corresponding normalized deposition rate is presented,

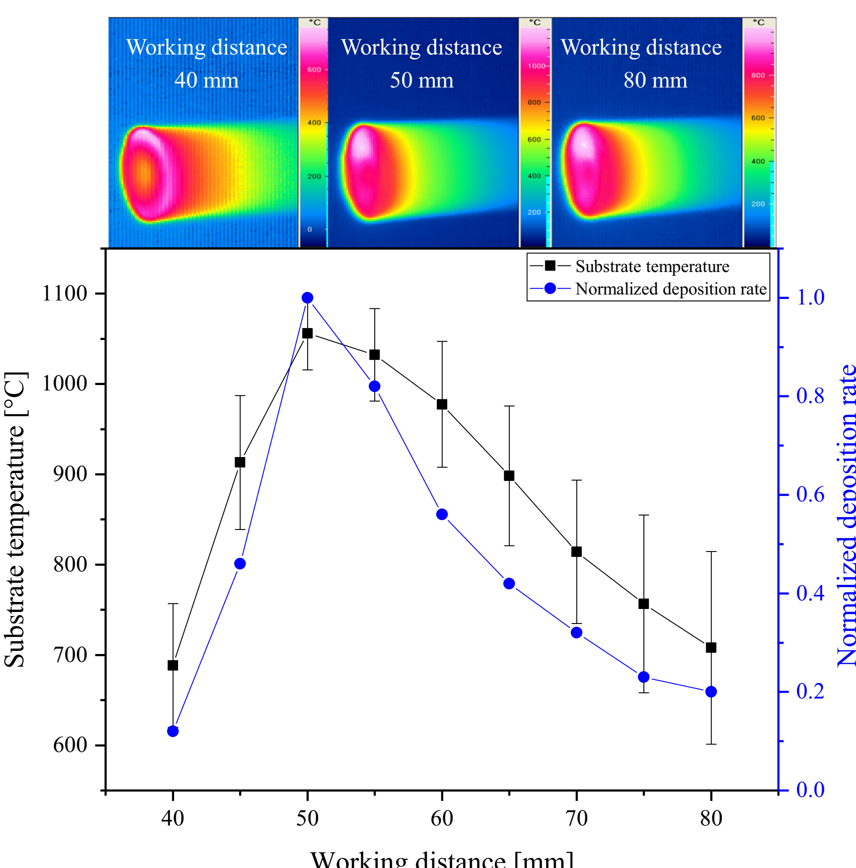

FIGURE 3 Substrate temperature and normalized deposition with respect to working distance. The shown error bars are representing the standard deviation for the surface temperature on the tip of the substrate with the associated mean values

which was investigated to obtain optimal deposition parameters. The normalized deposition rate is defined as the deposition rate of the individual test in relation to the maximum achieved deposition rate of the test series. The deposition rate was determined by evaluating the mass of the preform rod before and after deposition for a defined deposition time.

The maximum deposition rate is found at 50-mm working distance, corresponding to the highest substrate temperature. Working distances below 50 mm lead to strong substrate cooling caused by increased spraying impulse from the two-component jet. The spraying impulse creates a temperature dip at the center of the substrate tip, which can be seen in the related IR camera frame in Figure 3 for a working distance of 40 mm. The expected decrease in substrate temperature for increased working distances leads to decreased deposition rates, which coincides well with previous studies showing the strong correlation between surface temperature and deposition rate.[25]

3.3 | Results of plasma-deposited samples

Plasma-deposited samples doped with Al_2O_3 and Yb_2O_3 were prepared using TEOS as an Si precursor and are analyzed in terms of homogeneity aspects with EPMA and Raman spectroscopy. Comparable doping concentrations have been reported in a previous study.[25]

3.3.1 | Results of EPMA analysis

Plasma deposition of SiO_2 doped with Al_2O_3 and Yb_2O_3 was carried out with a target concentration of 3-mol% Al_2O_3 and 0.3-mol% Yb_2O. The samples were deposited with an optimized parameter set, using 3 kW of consumed microwave power for a deposition time of 30 min, a precursor flow rate of 2 g/min, a working distance of 50 mm, and an oxygen flow rate of 12 slm, with a maximum surface temperature of 1100°C. Exemplary results of the deposited material are shown in Figure 4.

The deposited samples were not fully vitrified during the process. Instead, a porous soot body deposition with a measured specific surface area (BET method) of 56 m^2/g, a mass of 3.45 g, and a sintering grade of around 30% referred to pure dense silica with 2.2 g/cm^3 was achieved. With the current setup, a maximum power level of 3 kW is available, rendering it challenging to fully vitrify the sample during the process, due to significant substrate cooling caused by the incoming two-component jet flow.

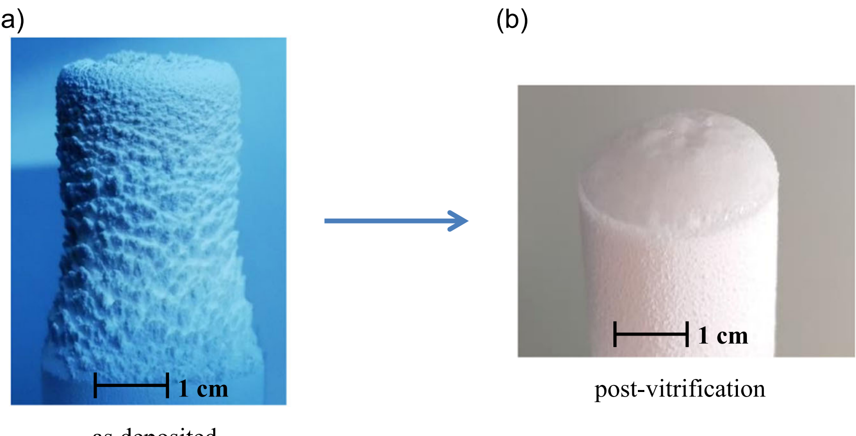

FIGURE 4 Plasma-deposited sample: (a) as-deposited and (b) after vitrification with plasma torch

Direct vitrification during deposition can only be obtained with substrate temperatures above 2000°C.[27,33,34]

For EPMA and Raman spectroscopic analysis, the samples were post-vitrified from the front surface in pure oxygen plasma at 3-kW microwave power at atmospheric pressure without injection. This step was necessary to flatten the surface of the samples to ensure comparable measuring conditions. Post-vitrification rendered an increased bubble formation. To circumvent this unfavorable bubble formation, an in-situ vitrification via upscaling to a more powerful microwave plasma system (15 kW) is envisioned.

Nevertheless, depending on the state of densification of the plasma-deposited material, several post-processing steps can be applied to obtain transparent, bubble-free, and fully densified preform material, including green body formation processing, followed by thermal post-processing via MCVD lathe or gas pressure sintering. Consequently, this preform material can be integrated in a preform ready for fiber drawing by the rod-in-tube or stack-and-draw technique.

BSE images revealed no visual phase separations and segregations on the micrometer scale, as shown in Figure 5. The black spots were identified as bubbles, which formed during vitrification with the pure oxygen plasma at atmospheric pressure.

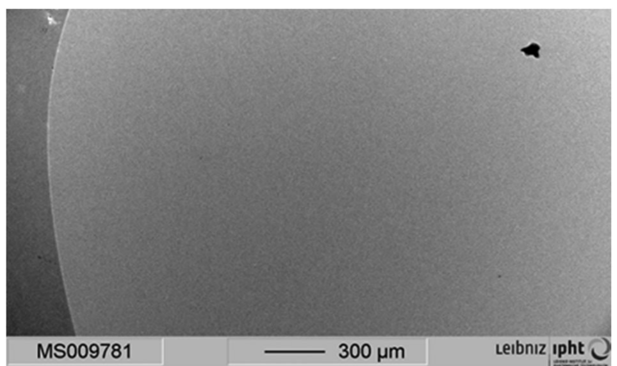

FIGURE 5 Backscattered electron image of polished and vitrified plasma-processed sample

An exemplary Al_2O_3 and Yb_2O_3 concentration radial sample profile, as derived from EPMA line scan, is shown in Figure 6a. For a better comparison, the scaling factor in the diagrams remains the same for both dopants. To quantitatively describe the dopant homogeneity of Al_2O_3 and Yb_2O_3, the data are transferred into a histogram, as shown in Figure 6b, depicting the mean value (μ) and the standard deviation (σ).

The line scan data across the sample diameter indicate good homogeneity of the sample for both Al_2O_3 and Yb_2O_3, as depicted in Figure 6a. The maximum molar fluctuation, Δmax, for Al_2O_3 is at 0.09 mol%, as depicted. Figure 6b reveals a mean value μ of 3.02 mol% with a corresponding standard deviation σ of 0.015 mol%. For Yb_2O_3, the dopant homogeneity is around four times better than that for Al_2O_3, as shown in Figure 6a, with a maximum molar fluctuation, Δmax, of 0.019 mol%. The standard deviation σ with 0.004 mol% is around three times lower than that for Al_2O_3, as shown by the smaller half-width depicted in the histogram curve in Figure 6b.

3.3.2 | Results of Raman spectroscopy

The obtained Raman scattering spectra from line scans are collected and averaged to one spectrum with a corresponding maximum fluctuation for intensity and frequency, as shown in Figure 7, indicated by the green bar. Only minor fluctuations are observed, indicating excellent structural homogeneity, corresponding quite well to EPMA measurement observations.

The band shape obtained is characteristic for alumina-doped silica, confirming that a fully vitrified network is formed.[35] The low-frequency band at around 430/cm is related to rocking and symmetric bending motions of bridging oxygen (BO) species.[36] The defect

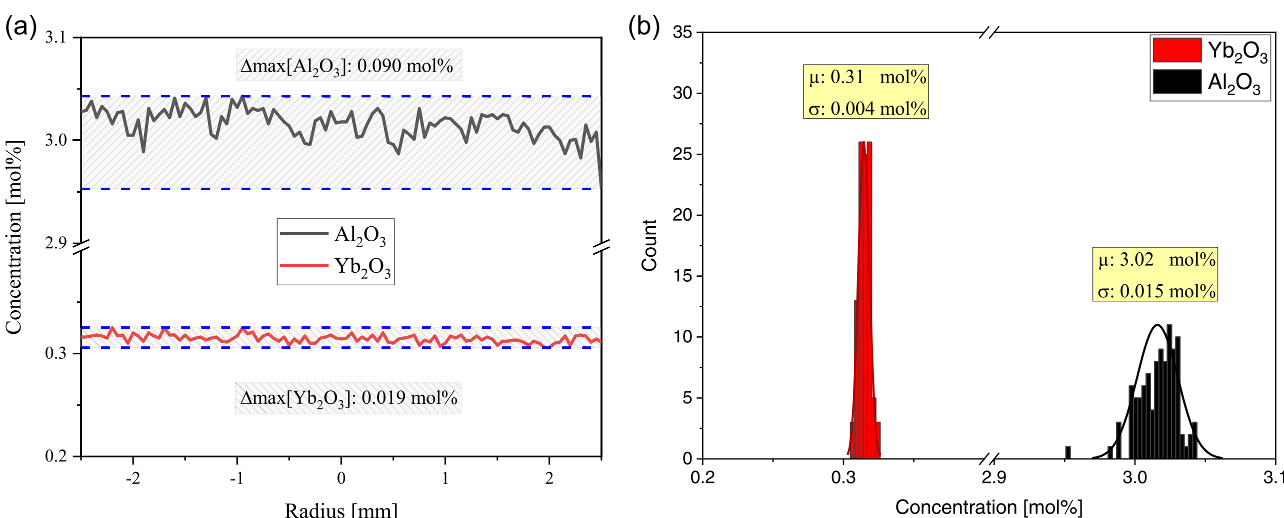

FIGURE 6 Radial Al_2O_3 and Yb_2O_3 distribution for an exemplary plasma-processed sample with the target concentration of 3 mol% Al_2O_3 and 0.3 mol% Yb_2O_3; (a) electron probe microanalysis line scan and (b) histogram for the dopant distribution

bands obtained at 490/cm (D_1) and 600/cm (D_2) are related to symmetric BO bending vibrations in 4- and 3-membered rings, respectively.[37,38] The mid-frequency band at about 800/cm results from the motion of Si atoms in their tetrahedral oxygen cage.[39] The high-frequency bands between 1050 and 1250/cm are attributed to Si–O stretching vibrations of tetrahedral SiO_4 groups.[40] Deviations in the Al_2O_3 concentration will lead to a change of the relative intensities for both D_1 and D_2 peaks, as observed in the study of Ando et al.,[35] indicating a change of the glass structure. The frequency band at 1050–1250/cm is also affected by Al_2O_3 variations, suggesting that an interconnected Si–O–Al network is built.[40]

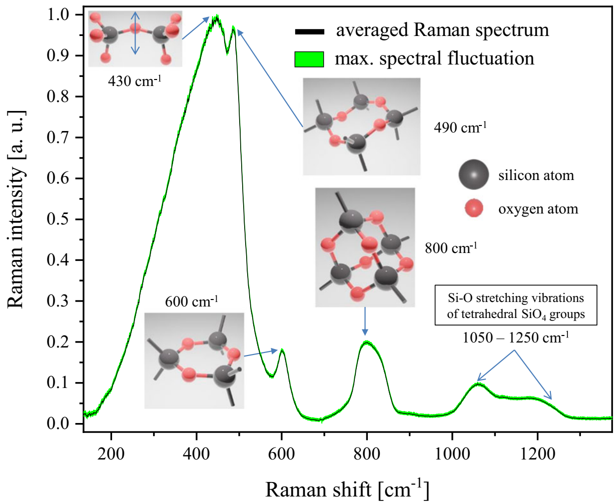

FIGURE 7 Raman scattering spectra of a plasma-deposited sample with 3 mol% Al_2O_3 and 0.3 mol% Yb_2O_3

3.4 | Comparison of radial dopant homogeneity with the well-established high-temperature preform fabrication technology Repusil

For an appropriate comparison, a representative plasma-processed sample is compared with an exemplary Repusil sample with a stoichiometric ratio close to 10:1 for Al_2O_3:Yb_2O_3.

In Figure 8a the EPMA line scan results for Repusil and plasma-processed sample are presented, with the corresponding histograms in Figure 8b showing the dopant distribution for Al_2O_3 and Yb_2O_3. For an improved comparison, the scaling factor in the diagrams remains the same for both dopants. The plasma-processed sample and the Repusil-processed sample are displayed again with a target concentration of 3 mol% for Al_2O_3. The Yb_2O_3 target concentration for the Repusil-processed sample is 0.25 mol %, and for the plasma-processed sample, it is 0.30 mol%. Comparing the Al_2O_3 line scan results of the Repusil sample with the plasma-processed sample in Figure 8a, the maximum molar fluctuation, Δmax, is about four times lower for the plasma-processed sample, indicating superior homogeneity. Moreover, the Yb_2O_3 profile of the plasma-processed sample is around 2.5 times more homogeneous than the Repusil-processed sample while comparing the maximum molar fluctuations, Δmax.

In Figure 8b the dopant distribution for Al_2O_3 and Yb_2O_3 derived from EPMA line scan is displayed for both the Repusil- and plasma-processed sample. By comparing the Al_2O_3 histogram curves, the plasma-processed sample shows about 4.5 times better homogeneity with respect to the specified standard deviation σ, demonstrating a

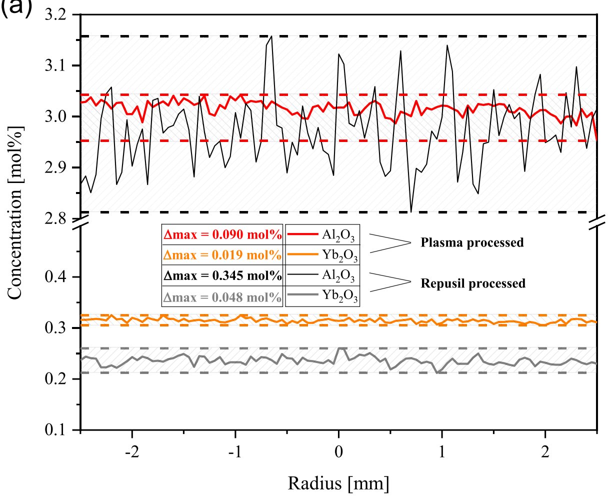

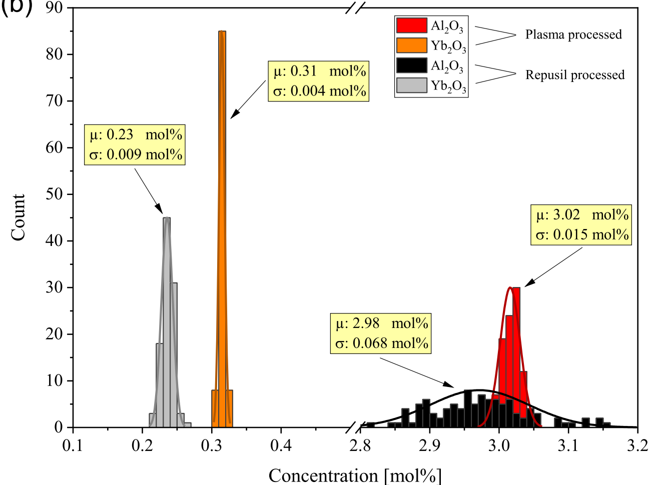

FIGURE 8 Radial Al_2O_3 and Yb_2O_3 distribution for plasma- and Repusil-processed samples with different target concentrations; (a) electron probe microanalysis line scans and (b) histograms for dopant distribution

considerably smaller half-width (red curve). For Yb_2O_3, the dopant fluctuation of the plasma-processed sample is around two times better than that for the Repusil-processed sample, correlating the standard deviations σ for each process.

Significant dopant homogeneity is required to achieve low variations in the refractive index profile (neglecting any fiber drawing induced effects). By using the available EPMA radial concentration profiles for both Al_2O_3 and Yb_2O_3, theoretical refractive index profiles are derived from the molar fractions c[mol%] and the refractive index increment presented in References [29,41].

$$\Delta n \times 10^4 = 67 \times cYb_2O_3 + 22 \times cAl_2O_3. \tag{1}$$

The fluctuations in concentrations sum up as fluctuations in the refractive index distribution. The results are plotted in Figure 9.

Thus, the calculated maximum fluctuations, $\Delta n_{\max}$, are superior for the plasma-processed sample, which are around three times lower as compared with the Repusil-processed sample, indicating excellent refractive index homogeneity, as displayed in Figure 9a. Figure 9b presents the refractive index distribution with the mean value $\mu_{\Delta n}$ and the standard deviation $\sigma_{\Delta n}$ for the plasma- and Repusil-processed sample. The refractive index fluctuations, derived from standard deviation $\sigma_{\Delta n,}$ are about 3.5 times lower for the plasma-processed sample, referring to superior refractive index homogeneity.

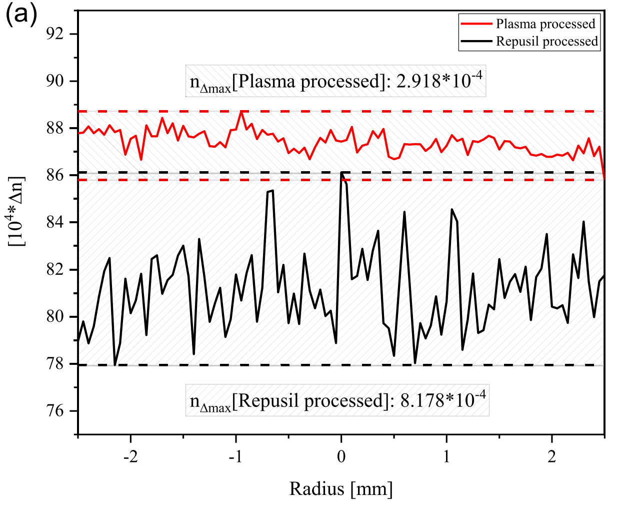

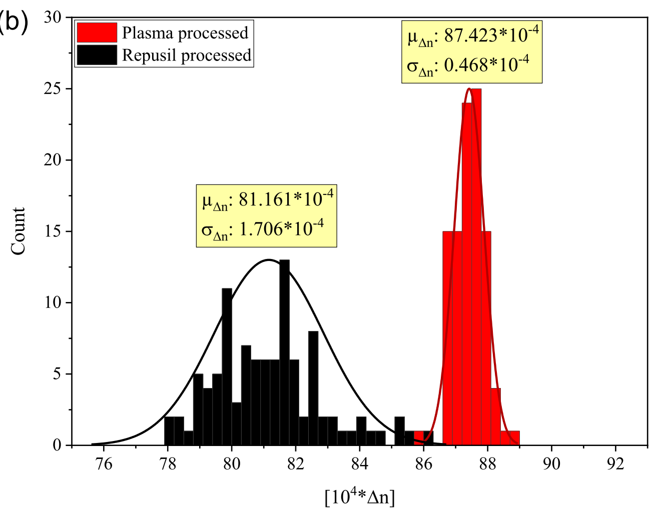

FIGURE 9 Calculated refractive index variations across sample radius for plasma- and measured Repusil-processed sample; (a) line scans and (b) histograms for refractive index distribution

4 | CONCLUSION AND OUTLOOK

An innovative approach based on microwave plasma at atmospheric pressure has been developed for the deposition of homogeneously RE-doped material for fiber laser preforms. Compared with established preform fabrication technologies, the new approach is eligible to extend the achievable active core specifications to maximum RE doping level, core diameter, and homogeneity of dopant distribution. Up to now, the Repusil process has been considered as the best choice to fabricate actively doped cores with large diameters and a good core material homogeneity for excellent large mode area fibers. With the plasma-based approach, specifications such as the maximum doping levels for RE as well as the overall dopant distributions can be significantly improved.

Exemplary Raman and EPMA analyses on plasma post-vitrified samples demonstrate radial doping homogeneity superior to comparable Repusil samples.

The material density of the plasma-deposited bulk material strongly depends on the substrate temperature during plasma deposition. In the present setup, microwave power is limited up to 3 kW, allowing for substrate temperatures <2000°C. For bubble-free in-situ vitrification, the energy output needs to be higher, which in the future will be solved by installation of a microwave system with a higher input power.

Therefore, the plasma procedure described in this paper significantly extends the present state-of-the-art large-core dopant homogeneity, as defined by the Repusil process with its unique features.

ACKNOWLEDGMENTS

This study is a part of the project *PlasFaser: Development of a plasma-based synthesis of novel multicomponent glasses for high-performance optical fibers*, financed by the Leibniz Association (SAW-2017-IPHT-1). Parts of the work have received funding from the European Research Council (ERC) under the European Union's Horizon 2020 research and innovation program (Lothar Wondraczek, ERC grant UTOPES, GRANT AGREEMENT No. 681652). Open access funding enabled and organized by Projekt DEAL.

CONFLICT OF INTERESTS

The authors declare that there are no conflict of interests.

ORCID

Tom Trautvetter http://orcid.org/0000-0003-3187-9460
Jan Schäfer https://orcid.org/0000-0002-0652-5057

REFERENCES

[1] G. P. Agrawal, *Nonlinear fiber optics*, Elsevier Science, Burlington, VT **2013**.

[2] C. Jauregui, J. Limpert, A. Tünnermann, *Nat. Photonics* **2013**, *7*(*11*), 861867.

[3] A. Méndez, T. F. Morse, *Specialty Optical Fibers Handbook*, Academic Press, Amsterdam, Boston **2007**, 840.

[4] F. Tosco, *Fiber Optic Communications Handbook*, Tab Books, Blue Ridge Summit, PA **1990**.

[5] P. Dragic, J. Ballato, A. Ballato, S. Morris, T. Hawkins, P.-C. Law, S. Ghosh, M. C. Paul, *Opt. Mater. Express* **2012**, *2*(*11*), 1641.

[6] K. Schuster, S. Unger, C. Aichele, F. Lindner, S. Grimm, D. Litzkendorf, J. Kobelke, J. Bierlich, K. Wondraczek, H. Bartelt, *Adv. Opt. Technol.* **2014**, *3*(*4*), 447.

[7] J. B. MacChesney, D. J. DiGiovanni, *J. Am. Ceram. Soc.* **1990**, *73*(*12*), 3537.

[8] M. Saha, A. Pal, M. Pal, C. Guha, R. Sen, *J. Lightwave Technol.* **2015**, *33*(*17*), 3533.

[9] J. E. Townsend, S. B. Poole, D. N. Payne, *Electron. Lett.* **1987**, *23*(*7*), 329.

[10] M. Leich, F. Just, A. Langner, M. Such, G. Schötz, T. Eschrich, S. Grimm, *Opt. Lett.* **2011**, *36*(*9*), 1557.

[11] D. Litzkendorf, S. Grimm, K. Schuster, J. Kobelke, A. Schwuchow, A. Ludwig, J. Kirchhof, M. Leich, S. Jetschke, J. Dellith, J.-L. Auguste, G. Humbert, *Int. J. Appl. Glass Sci.* **2012**, *3*(*4*), 321.

[12] D. Levy, M. Zayat, *The Sol-Gel Handbook: Synthesis, Characterization, and Applications*, Wiley, Berlin **2015**, 1616.

[13] C. J. Brinker, G. W. Scherer, *Sol-Gel Science*, Elsevier Science, Burlington, VT **1990**.

[14] A. Baz, H. E. Hamzaoui, I. Fsaifes, G. Bouwmans, M. Bouazaoui, L. Bigot, *Laser Phys. Lett.* **2013**, *10*(*5*), 55106.

[15] A. Sarkar, F. Kirkbir, S. Raychaudhuri, *Key Eng. Mater.* **1998**, *150*, 153.

[16] V. Reichel, H. Baierl, A. Kalide, A. Scheffel, J. Dellith, K. Schuster, *Proc. SPIE* **2018**.*10528*, .

[17] A. Langner, G. Schötz, M. Such, T. Kayser, V. Reichel, S. Grimm, J. Kirchhof, V. Krause, G. Rehmann, *Proc. SPIE* **2008**, *6873*.

[18] A. Schutze, J. Y. Jeong, S. E. Babayan, J. Park, G. S. Selwyn, R. F. Hicks, *IEEE Trans. Plasma Sci.* **1998**, *26*(*6*), 1685.

[19] R. W. Smith, D. Wei, D. Apelian, *Plasma Chem. Plasma Process.* **1989**, *9*(*1*), 135.

[20] J. Salge, *Surf. Coat. Technol.* **1996**, *80*, 1.

[21] J. J. Cuomo, S. M. Rossnagel, W. D. Westwood, *Handbook of Plasma Processing Technology*, Noyes Publications, Park Ridge, NJ **1990**, 546.

[22] M. Leins, K.-M. Baumgärtner, M. Walker, A. Schulz, U. Schumacher, U. Stroth, *Plasma Processes Polym.* **2007**, *4*(*1*), 493497.

[23] M. Moisan, J. Pelletier, *Microwave Excited Plasmas*, Elsevier, Amsterdam **1999**.

[24] O. P. Solonenko, *Plasma Torches, Basic Studies and Design*, Cambridge Interscience Publishing, Cambridge **2000**.

[25] T. Trautvetter, H. Baierl, V. Reichel, A. Scheffel, J. Dellith, D. Köpp, F. Hempel, M. Baeva, R. Methling, R. Foest, L. Wondraczek, K. Wondraczek, H. Bartelt, *Proc. SPIE* **2019**, *10914*.

[26] R. Methling, F. Hempel, M. Baeva, T. Trautvetter, H. Baierl, R. Foest, *Plasma Phys. Technol.* **2019**, *6*, 243. https://doi.org/10.14311/ppt.2019.3.243

[27] I. G. Sayce, N. Stocksfield, R. B. Coapes, A. Mundy, *WO 2011/107430*, **2011**.

[28] S. Jetschke, S. Unger, M. Leich, J. Kirchhof, *Appl. Opt.* **2012**, *51*(*32*), 7758.

[29] S. Unger, A. Schwuchow, J. Dellith, J. Kirchhof, *Opt. Mater. Express* **2020**, *10*(*4*), 907.

[30] M. Baeva, F. Hempel, H. Baierl, T. Trautvetter, R. Foest, D. Loffhagen, *J. Phys. D: Appl. Phys.* **2018**, *51*(*38*), 385202.

[31] J. Curry, G. Herzberg, *Ann. Phys.* **1934**, *411*(*7*), 800.

[32] M. W. Feast, *Proc. Phys. Soc. A* **1949**, *62*(*2*), 114.

[33] D. R. Sempolinski, M. Wasilewski, C. Yu, *EP0978486A1*, **2000**.

[34] H. Berthou, V. Neumann, H. E. Hintermann, *Surf. Coat. Technol.* **1993**, *61*(*1–3*), 164.

[35] M. F. Ando, O. Benzine, Z. Pan, J.-L. Garden, K. Wondraczek, S. Grimm, K. Schuster, L. Wondraczek, *Sci. Rep.* **2018**, *8*(*1*), 5394.

[36] N. Zotov, I. Ebbsjö, D. Timpel, H. Keppler, *Phys. Rev. B* **1999**, *60*(*9*), 6383.

[37] F. L. Galeener, *J. Non-Cryst. Solids* **1982**, *49*(*1*), 53.

[38] R. M. Martin, F. L. Galeener, *Phys. Rev. B* **1981**, *23*(*6*), 3071.

[39] P. McMillan, *Am. Mineral.* **1984**, *69*, 622.

[40] M. Okuno, N. Zotov, M. Schmücker, H. Schneider, *J. Non-Cryst. Solids* **2005**, *351*(*12–13*), 1032.

[41] J. Kirchhof, S. Unger, A. Schwuchow, S. Jetschke, B. Knappe, *Proc. SPIE* **2005**, 261. https://doi.org/10.1117/12.590021

How to cite this article: Trautvetter T, Schäfer J, Benzine O, et al. Plasma-based VAD process for multiply doped glass powders and high-performance fiber preforms with outstanding homogeneity. *Plasma Process Polym*. 2020;17:e2000140. https://doi.org/10.1002/ppap.202000140